Coexistence of superconductivity and topological phase in kagome metals ANb_3Bi_5 (A = K, Rb, Cs)

Check for updates

Jianguo Si [1,2], Lanting Shi[3], Bozhu Chen[1,2], Huanhuan Yang[1,2], Jiyu Xu [1,2] ✉, Miao Liu [1,2,4] ✉ & Sheng Meng [1,2,4] ✉

The AV_3Sb_5 prototype kagome materials have been demonstrated as a versatile platform for exploring exotic properties in condensed matter physics, including charge density waves, superconductivity, non-trivial electron topology, as well as topological superconductivity. Here we identify that ANb_3Bi_5 (A = K, Rb, Cs) exhibit non-trivial coexisting superconductivity and topological properties via first-principles calculations. The negative formation energy and the absence of imaginary phonon dispersion demonstrate both thermodynamics and dynamics stabilities of ANb_3Bi_5 (A = K, Rb, Cs) under ambient conditions. By analytically solving the Allen-Dynes-modified McMillan formula, the superconducting transition temperatures are predicted to be 2.11, 2.15 and 2.21 K for KNb_3Bi_5, $RbNb_3Bi_5$, and $CsNb_3Bi_5$, respectively. More importantly, the kagome materials proposed here can be classified into $\mathbb{Z}_2$ topological metals due to the non-trivial topological index and the obvious surface states around the Fermi level. Such coexistence of superconductivity and non-trivial band characters in ANb_3Bi_5 (A = K, Rb, Cs) offer us more insights to study the relationship between superconductivity and topological properties, and to design innate topological superconductors.

Materials with kagome lattice, composed of tiled corner-sharing triangles, have attracted enormous attention in recent decades due to its inherent geometrical frustration and strong correlations, inducing many exotic phenomena, such as spin liquid phase[1–3], magnetic topological states[4–7], chiral physics[8–10], unconventional superconductivity[8,9,11–14], *etc.* The genuine kagome materials host flat band in the entire Brillouin zone, Dirac point at K point and van Hove point (or saddle point) at M point. However, the relationship between the unique electronic structure and the corresponding exotic phenomena is still under hot debate for these kagome materials.

The V-based kagome metals AV_3Sb_5 (A = K, Rb, Cs) have been synthesized with a quasi-two-dimensional characteristic[15]. Subsequent studies have demonstrated that this family materials undergo the charge density wave (CDW) transitions in a temperature range form 80 to 102 K[9,13,16–20]. Further, this family materials also undergo the superconducting transitions at 0.93, 0.92 and 2.5 K for KV_3Sb_5, RbV_3Sb_5 and CsV_3Sb_5[9,13–17] respectively, and the superconducting transition temperature shows double-dome-liked pressure-dependent behavior under high pressure[20–22]. In addition, the nontrivial band characteristics are confirmed by angle resolved

photoemission spectroscopy (ARPES), Shubnikov-de Haas oscillation measurements and theoretical calculations[15–18,23]. The coexistence of superconductivity and nontrivial band structures are necessary for the realization of topological superconductor and Majorana zero mode[24,25]. For example, the Majorana bound states have been experimentally detected in CsV_3Sb_5[13], where the Majorana bound states in the vortex core are proved to exist only with chiral *p*-wave pairing[14].

Inspired by the fascinating properties of kagome metals AV_3Sb_5 (A = K, Rb, Cs), extensive experimental and computational works have been performed to design and synthesize novel kagome materials with an AV_3Sb_5-type isostructure. For examples, the high-throughput first-principles calculations are used to enlarge the family of AV_3Sb_5 prototype materials through element species substitution[26,27],and the potential topological superconductivity and CDW orders are also predicted simultaneously[27–29]. Recently, the ATi_3Bi_5 (A = Cs, Rb) family materials have been experimentally synthesized[30–32], which exhibit the orbital-selective nematic order[30], nontrivial band topology[31,32], superconducting transition with a critical temperature of 4.8 K[30] and the pressure-induced double-dome

¹Songshan Lake Materials Laboratory, Dongguan, Guangdong 523808, People's Republic of China. ²Beijing National Laboratory for Condensed Matter Physics and Institute of Physics, Chinese Academy of Sciences, Beijing 100190, People's Republic of China. ³Institute of High Energy Physics, Chinese Academy of Science, Beijing 100049, People's Republic of China. ⁴University of Chinese Academy of Sciences, Beijing 100049, People's Republic of China.
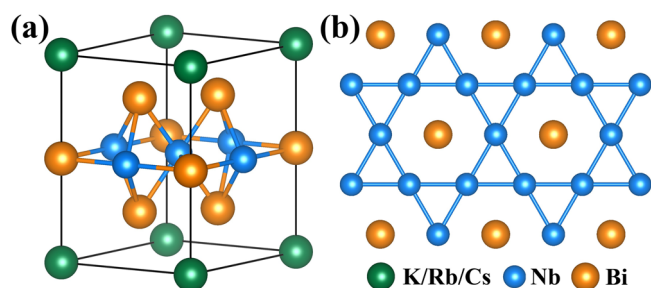✉e-mail: jiyuxu@iphy.ac.cn; mliu@iphy.ac.cn; smeng@iphy.ac.cn

Fig. 1 | Crystal structure of $A\text{Nb}_3\text{Bi}_5$ (A = K, Rb, Cs). a Side view of the crystal structure of $A\text{Nb}_3\text{Bi}_5$. **b** Top view of the kagome layer. The green, blue, and orange balls indicate the alkali metal A (A = K, Rb, Cs), transition-metal Nb and Bi atoms, respectively.

Table 1 | Crystal parameters (in Å) and the formation energy (in meV) of $A\text{Nb}_3\text{Bi}_5$ (A = K, Rb, Cs)

Compound	a	c	$E_{formation}$ or Reference
KNb$_3$Bi$_5$	5.84	9.15	-59.9
	5.89	9.59	26
RbNb$_3$Bi$_5$	5.85	9.28	-79.6
	5.89	9.71	26
CsNb$_3$Bi$_5$	5.86	9.44	-104.6
	5.91	9.87	26
CsTi$_3$Bi$_5$	5.84	9.30	30

superconductivity[33]. The fascinating electronic and transport properties of $A\text{V}_3\text{Sb}_5$ (A = K, Rb, Cs) and $A\text{Ti}_3\text{Bi}_5$ (A = Cs, Rb) materials imply the necessity of theoretically designing other $A\text{V}_3\text{Sb}_5$ prototype structures and in-depth interpretation from electronic structure calculations, which could also supply more insights for exploring unconventional properties in various condensed systems.

In this work, we predict another family of kagome metals $A\text{Nb}_3\text{Bi}_5$ (A = K, Rb, Cs) with the coexistence of superconductivity and non-trivial band topology. The formation energy and phonon dispersion calculations demonstrate the relatively excellent thermodynamical and dynamical stabilities. Based on the Allen-Dynes-modified McMillan formula[34,35], the superconducting transition temperatures for KNb$_3$Bi$_5$, RbNb$_3$Bi$_5$, and CsNb$_3$Bi$_5$ are predicted to be 2.11, 2.15 and 2.21 K, respectively. The calculated band structures without spin-orbit coupling (SOC) effect exhibit the characteristics of Dirac points, van Hove singularities and flat band in traditional kagome lattice. With SOC effect, the Dirac points are gapped, and all $A\text{Nb}_3\text{Bi}_5$ (A = K, Rb, Cs) family materials are predicted as $\mathbb{Z}_2$-topological metals. The coexistence of superconductivity and non-trivial band topology in $A\text{Nb}_3\text{Bi}_5$ (A = K, Rb, Cs) family materials reported here will spark further experimental investigations.

Results and discussion
Crystal structure of $A\text{Nb}_3\text{Bi}_5$
The $A\text{Nb}_3\text{Bi}_5$ family materials crystallize in a layered hexagonal structure with the space group $P6/mmm$ (No. 191), and can be constructed by partly element species substituting from $A\text{V}_3\text{Sb}_5$ or $A\text{Ti}_3\text{Bi}_5$. As shown in Fig. 1, the $A\text{Nb}_3\text{Bi}_5$ systems are formed by stacking Nb$_3$Bi$_5$ layers along c-axis via weak vdW interaction, where the alkali metal atoms can be regarded as inserted atoms between the Nb$_3$Bi$_5$ layers. The inserted alkali metal atoms are shown to play an important role in modulating the chemical potential, which means that the intercalation and deintercalation of alkali metal atoms will effectively shift the Fermi level without changing the dispersion of band structure[15]. The Bader charge analysis show the charge transfer effect in $A\text{Nb}_3\text{Bi}_5$ (A = K, Rb, Cs) materials in Supplementary Table 1. One can see that each alkali metal atom transfer ~ 0.75 electron to the adjacent Nb$_3$Bi$_5$ layers, close to that of $A\text{V}_3\text{Sb}_5$ (A = K, Rb, Cs)[15]. In Nb-Bi slab, the Nb atoms form a net kagome lattice. The fully relaxed crystal structure parameters are listed in Table 1. One can see that the in-plane parameters have almost no change with increasing atomic number of alkali metal, while the lattice parameters along c-axis increase by ~ 0.29 Å from K to Cs, which is consistent with the previous high-throughput work[26]. It can be seen that our calculated lattice constants are slightly smaller than the high-throughput calculation results, and the vdW corrections included here give more accurate description of interlayer interactions. Furthermore, we compare the calculated parameters of CsNb$_3$Bi$_5$ with experimentally synthesized CsTi$_3$Bi$_3$[30], and the difference between them is rather small, demonstrating the reliability of our calculations.

Thermodynamic stability of $A\text{Nb}_3\text{Bi}_5$
To evaluate the thermal stability of these components, we calculated the formation energy by

$$E_{formation} = \frac{E_{A\text{Nb}_3\text{Bi}_5} - E_A - 3E_{\text{Nb}} - 5E_{\text{Bi}}}{9}. \quad (1)$$

Here, $E_{A\text{Nb}_3\text{Bi}_5}$ is the total energy per formula cell. The E_A, E_{Nb} and E_{Bi} are the energy per atom for alkali metal A (A = K, Rb, Cs), transition metal Nb and Bi elemental substances, respectively. The alkali metal A (A = K, Rb, Cs) and the transition metal Nb atoms crystallize in a body-centered cubic phase with the space group of $Im\bar{3}m$[36,37], while the Bi atoms exhibit the space group of $R\bar{3}m$[38]. The calculated results in Table 1 show that the formation energies of these materials are all negative, demonstrating that $A\text{Nb}_3\text{Bi}_5$ family materials are thermodynamically stable. This agrees well with the previous high-throughput work[26], where the thermodynamic stability is evaluated by calculating the energy above hull. In addition, we also calculated formation energies with binary components as reactants in Supplementary Fig. 1. The results show that the $A\text{Nb}_3\text{Bi}_5$ (A = K, Rb, Cs) family materials can be synthesized with their binary counterparts except for KBi$_2$, RbBi$_2$ and CsBi$_2$.

Dynamic stability and Superconductivity of $A\text{Nb}_3\text{Bi}_5$
Phonon dispersion is a key method to evaluate the dynamic stability of a system. The calculated phonon dispersions of $A\text{Nb}_3\text{Bi}_5$ are shown in Fig. 2. One can see that there is no imaginary phonon mode for these three materials, indicating the structures are all dynamically stable. The maximums of phonon frequency are relatively close for these three materials. The phonon dispersion can be divided into two regions according to the vibration frequency. In the high-frequency region ($\omega > 125 \text{ cm}^{-1}$), the phonons are composed of the vibration modes of Nb atoms. Comparing to the CsV$_3$Sb$_5$ and CsM_3Te$_5$ (M = Ti, Zr, Hf), the flat modes dominated by the out-of-plane vibration modes of the transition metals become more dispersive for $A\text{Nb}_3\text{Bi}_5$[28,39]. For the low-frequency region, the phonons are formed by mixing the vibrational modes of atoms alkali metal A (A = K, Rb, Cs) and Bi atoms. The K atoms have the smallest mass in KNb$_3$Bi$_5$, but the interaction between K atoms and Nb$_3$Bi$_5$ layers is relatively weak. Therefore, the K atoms exhibit the lower vibration frequency in Fig. 2a. This stronger localization for RbNb$_3$Bi$_5$ and CsNb$_3$Bi$_5$ in frequency space can be attributed to the fact that the less charge transfer from Rb/Cs atom and the enlargement of layer space make the interaction between alkali metal atoms and Nb$_3$Bi$_5$ layers weaker. When it comes to RbNb$_3$Bi$_5$ and CsNb$_3$Bi$_5$, the vibration modes hybridization gradually decreases and the vibration modes of Rb and Cs are more localized in frequency space. In addition, one can see that the lowest acoustic branch dominated by the out-of-plane vibrations of Bi atoms shows significant softening, which may induce larger electron-phonon coupling effect and a structural instability when the system temperature is down to a critical value, such as CDW transition. Therefore, we take the KNb$_3$Bi$_5$ as an example to check the temperature effect on phonon dispersion, and the phonon dispersion of KNb$_3$Bi$_5$ is recalculated via changing the Fermi-Dirac smearing factor σ. Here, σ corresponds to the
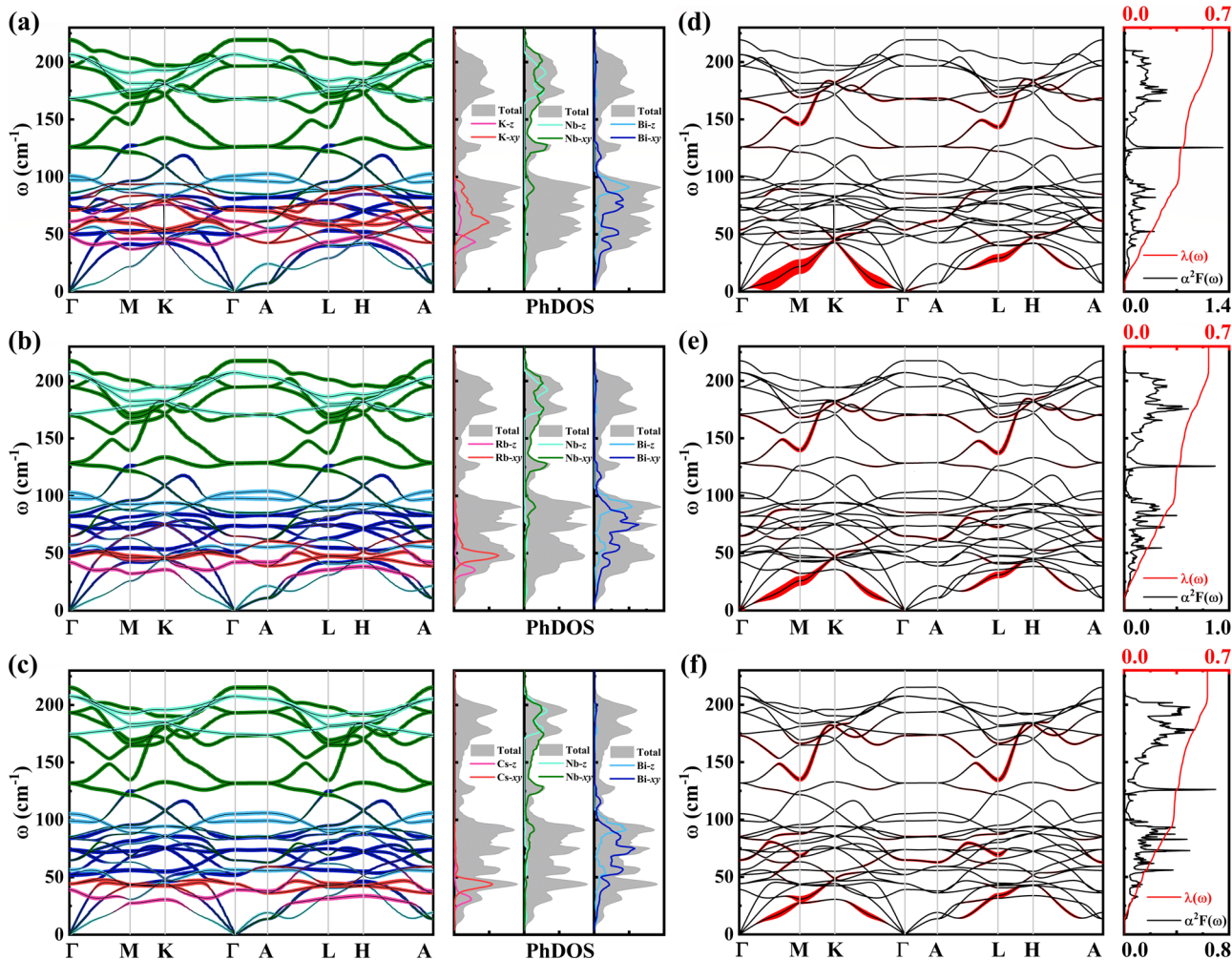
Fig. 2 | Phonon dispersions of ANb$_3$Bi$_5$ (A = K, Rb, Cs). Phonon dispersions weighted by different atomic vibrational modes of (**a**) KNb$_3$Bi$_5$, (**b**) RbNb$_3$Bi$_5$ and (**c**) CsNb$_3$Bi$_5$, respectively. The right panels of (**a**–**c**) are the total (gray-shaded zone) and vibrational mode-resolved (colored lines) phonon density of states (PhDOS). Phonon dispersions weighted by the magnitude of the phonon linewidth for (**d**) KNb$_3$Bi$_5$, (**e**) RbNb$_3$Bi$_5$, and (**f**) CsNb$_3$Bi$_5$, respectively. The right panels are the Eliashberg spectral function $\alpha^2 F(\omega)$ (black line), and the integrated strength of electron-phonon coupling $\lambda(\omega)$ (red line).

electronic temperature of electronic subsystem[40], and can be used to describe the CDW evaluation[41,42]. As shown in Supplementary Fig. 2, there is no imaginary modes for all calculated phonon dispersions, indicating that the system is stable under these temperatures and thus no CDW transition occurs.

Encouraged by the discovery of superconductivity in AV$_3$Sb$_5$ (A = K, Rb, Cs) and ATi$_3$Bi$_5$ (A = Rb, Cs), a series of experimental and theoretical works have been performed to explore the other kagome-based superconducting materials, as listed in Supplementary Table 2. Here, we estimate the possible superconductivity in ANb$_3$Bi$_5$ family materials according to the Allen-Dynes modified McMillan formula[34,35]. The superconducting transition temperature T_c is calculated as

$$T_c = \frac{\omega_{\log}}{1.2} \exp\left(-\frac{1.04(1+\lambda)}{\lambda - \mu^* - 0.62\lambda\mu^*}\right) \quad (2)$$

where the ω_{log} is logarithmically averaged characteristic phonon frequency, which is defined as

$$\omega_{\log} = \exp\left(\frac{2}{\lambda} \int \frac{d\omega}{\omega} \alpha^2 F(\omega) \log \omega\right). \quad (3)$$

The integrated electron-phonon coupling strength can be evaluated by

$$\lambda(\omega) = 2 \int \frac{\alpha^2 F(\omega)}{\omega} \, d\omega. \quad (4)$$

The total electron-phonon coupling constant λ used in Eq. (2) is $\lambda(\omega_{max})$, where ω_{max} is the maximum of the phonon frequency. The $\alpha^2 F(\omega)$ mentioned above is the Eliashberg spectral function and can be calculated according to the following formula:

$$\alpha^2 F(\omega) = \frac{1}{2\pi N(E_F)} \sum_{q\nu} \delta(\omega - \omega_{q\nu}) \frac{\gamma_{q\nu}}{\hbar\omega_{q\nu}}, \quad (5)$$

where $\omega_{q\nu}$ are phonon frequencies, $\gamma_{q\nu}$ is phonon linewidth as described by

$$\begin{aligned}
\gamma_{q\nu} = & \ 2\pi\omega_{q\nu} \sum_{ij} \int \frac{d^3 k}{\Omega_{BZ}} |g_{q\nu}(k,i,j)|^2 \\
& \times \delta(\varepsilon_{q,i} - \varepsilon_F)\delta(\varepsilon_{k+q,j} - \varepsilon_F).
\end{aligned} \quad (6)$$

Here, the $g_{q\nu}(k,i,j)$ is the matrix of the electron phonon coupling and $\varepsilon_{q,i}$ is the Kohn-Sham energy. The calculated Eliashberg spectral (black line) and integrated electron-phonon coupling strength (red line) are plotted in the right panel of Fig. 2d–f. Similar to CsM$_3$Te$_5$, the distributions of Eliashberg

Fig. 3 | Band structures without SOC for ANb_3Bi_5 (A = K, Rb, Cs). Orbital resolved band structure and density of states without the SOC effect for (**a**) KNb_3Bi_5, (**b**) $RbNb_3Bi_5$ and (**c**) $CsNb_3Bi_5$, respectively. The bands crossing the Fermi level are illustrated by the black line. The black and blue arrows are the Dirac points (DP) and van Hove singularities (vHs).
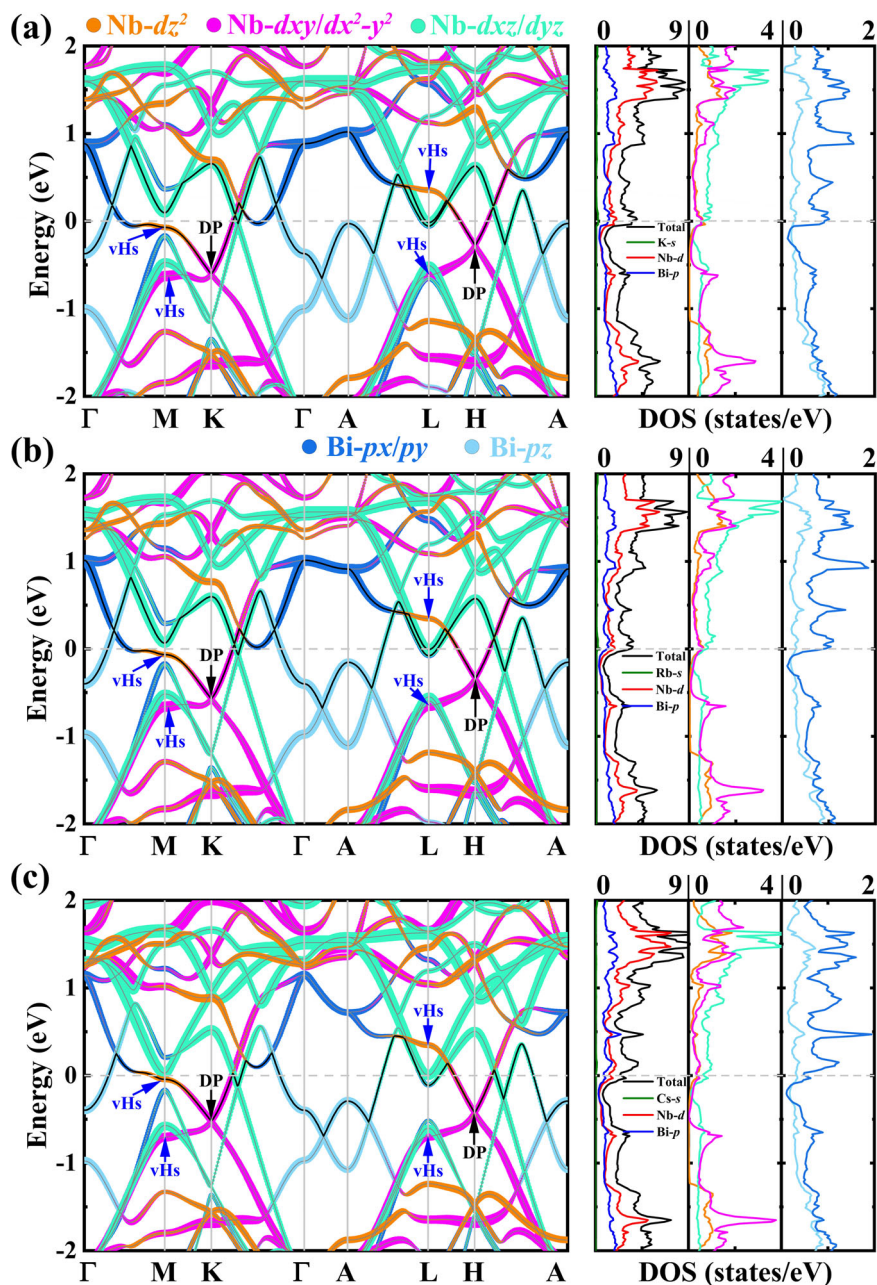
spectral function $\alpha^2F(\omega)$ are non-negligible at the high frequency region[28]. But for ANb_3Bi_5, the electron-phonon coupling from the high-frequency region ($\omega > 125$ cm^{-1}) reach 37 %, which can be attributed the soften modes around M/L points in ANb_3Bi_5. To explain this, we plotted the phonon dispersions weighted by the magnitude of the phonon linewidth (and consequently to the electron phonon coupling strength) in Fig. 2d–f. One can see that there are two obvious soften modes around M/L points. According to Eq. (4), these soften modes can induce stronger electron-phonon coupling effect. By comparing the phonon spectrum weighted by vibration modes of different atoms in Fig. 2a–c and weighted by the magnitude of the phonon linewidth in Fig. 2d–f, we can determine that the soften modes around M/L points result from the in-plane vibration modes of Nb-xy. In other words, the in-plane vibration modes of Nb have significant contribution to the electron-phonon coupling effect, as well as the superconductivity. For the lowest acoustic branch dominated by the out-of-plane vibrations of Bi atoms, the stronger electron-phonon coupling effect is clearly shown in Fig. 2d–f. The calculated total electron-phonon

coupling constant λ are 0.548, 0.552 and 0.556 for KNb_3Bi_5, $RbNb_3Bi_5$ and $CsNb_3Bi_5$, respectively. Thus, this family materials can be classified as weak superconductors. The μ^* in Eq. (2) is effective Coulomb pseudopotential, which has a significant impact on the value of T_c. We then check the influence of μ^* on T_c. As shown in Supplementary Fig. 3, T_c decreases with increase of μ^*. We used the value of μ^* of 0.1 to calculate T_c in all calculations. The corresponding superconducting transition temperatures T_c at ambient pressure are 2.11, 2.15 and 2.21 K, slightly higher than these of $CsTi_3Bi_5$ (1.85 K) and $RbTi_3Bi_5$ (1.92 K)[29]. It is worth noting that both the electron-phonon coupling constant λ and superconducting transition temperatures T_c are very close for these three materials, which further confirms that superconductivity is attributed to the in-plane vibration modes of Nb-xy and out-of-plane vibrations of Bi-z.

Electronic structures and topological properties of ANb_3Bi_5

Without the SOC effect, the calculated band structures of ANb_3Bi_5 are shown in Fig. 3a–c. There are two bands crossing the Fermi level for both
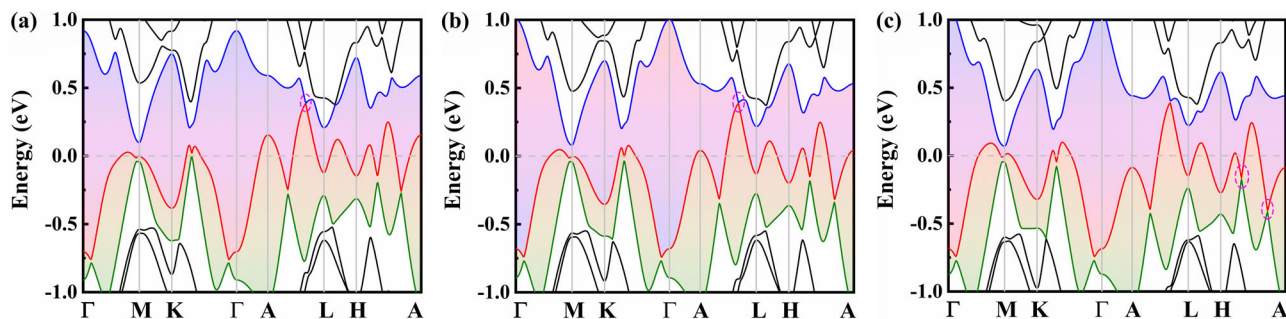
Fig. 4 | Band structures with SOC for ANb_3Bi_5 (A = K, Rb, Cs). Band structures with SOC effect for (**a**) KNb_3Bi_5, (**b**) $RbNb_3Bi_5$ and (**c**) $CsNb_3Bi_5$, respectively. The colored shadows illustrate the continuous band gaps along the whole high symmetry path. The pink ellipses indicate the minimum gap for each system.

KNb_3Bi_5 and $RbNb_3Bi_5$, while there is only one band crossing the Fermi level for $CsNb_3Bi_5$. For the Nb-based kagome materials KNb_3Bi_5, there are two symmetry-protected Dirac points located at K (-0.605 eV) and H (-0.276 eV) points, which are dominated by the in-plane orbitals of Nb d_{xy}/$d_{x^2-y^2}$. Considering that the inserted alkali metal A (A = K, Rb, Cs) plays an important role in charge transferring, the electronic structures near the Fermi level are barely changed by the removal of alkali metals[16]. We also calculated the band structure for the hypothetical compound Nb_3Bi_5 in Supplementary Fig. 4. It can be seen that the Dirac points are located at -0.141 eV, closer to the Fermi level. For ANb_3Bi_5, the band forming Dirac points also create four van Hove singularities (or saddle points) at M and L points. The two van Hove singularities with higher energy are mainly contributed by the orbitals of Nb d_{z^2}, while the lower two still result from the in-plane orbitals of Nb d_{xy}/$d_{x^2-y^2}$. This orbital composition of Dirac points and van Hove singularities is consistent with these of CsV_3Sb_5 and $CsTi_3Bi_5$[31,39,43]. The orbitals of Nb d_{xz}/d_{yz} contribute to several flat-band-liked bands along the whole high-symmetry path above the Fermi level (1.5 eV), while the orbitals of Nb d_{xy}/$d_{x^2-y^2}$ create several partly flat bands along MKΓ and LH directions. The similar orbital characters of flat band were also reported for CsV_3Sb_5[43]. Experimentally, the flat band, Dirac points and van Hove singularities are also partly observed in ARPES measurements of $CsTi_3Bi_5$ and CsV_3Sb_5[31,43]. As is well-known, the electrons around the Fermi level have significant contribution to superconductivity. We can see that the density of states (DOS) at the Fermi level mainly result from the d orbitals of Nb atoms and p orbitals of Bi atoms. The orbital-resolved DOS are calculated to obtain accurate orbital distribution. The orbitals of Nb d_{xz}/d_{yz} and Bi p_x/p_y contribute the most to the DOS at the Fermi level. As shown in Fig. 3b–c, the characters of electronic structures of $RbNb_3Bi_5$ and $CsNb_3Bi_5$ are particularly similar to that of KNb_3Bi_5, demonstrating that the difference of superconducting transition temperature in these three materials can be rather small.

For AV_3Sb_5 prototype kagome materials, the non-trivial topological properties are confirmed by theoretical calculations, ARPES and Shubnikov-de Haas oscillation experiments[15–18,23]. Here, we also investigate the topological properties via calculating the parity of the wave function at the time-reversal invariant momentum (TRIM) points and the surface states[44]. This method originates from the study of topological insulators, and recently it has been extended to the study of topological semimetals recently, such as YT_6Sn_6 (T = V, Nb, Ta)[45], RV_6Ge_6[46], etc.

The calculated band structures with SOC effect for ANb_3Bi_5 are drawn in Fig. 4. Comparing to the band structures without SOC effect, the band structures change dramatically due to the large atomic mass. There is only one band crossing the Fermi level. For the bands around the Fermi level, the continuous band gaps are opened and plotted by the colored shadows in Fig. 4a–c. The Dirac-like bands crossing at K and H points are gapped by 0.239 and 0.168 eV for KNb_3Bi_5, 0.233 and 0.164 eV for $RbNb_3Bi_5$, 0.211 and 0.158 eV for $CsNb_3Bi_5$, respectively. One can see that the SOC-induced gaps are quite close for these three materials, similar to the case of AV_3Sb_5 (A = K, Rb, Cs)[15]. This can be attributed to the fact that the bands around the

Table 2 | Parity of wave function at TRIMs and the $\mathbb{Z}_2$ indices of ANb_3Bi_5 (A = K, Rb, Cs)

Compound	Band Index	Parity				Product of parity				$\mathbb{Z}_2$
		Γ	3M	A	3L	Γ	3M	A	3L	
KNb_3Bi_5	I	−	+	+	+	+	−	−	−	1
	II	−	−	+	−	−	+	−	+	0
	III	−	+	+	−	+	+	−	−	0
$RbNb_3Bi_5$	I	−	+	+	+	+	−	−	−	1
	II	−	−	+	−	−	+	−	+	0
	III	−	+	+	−	+	+	−	−	0
$CsNb_3Bi_5$	I	−	+	+	+	+	−	−	−	1
	II	−	−	+	−	−	+	−	+	0
	III	+	+	+	−	−	+	−	−	1

Fermi level exhibit similar orbital characteristics. The narrowest gaps, highlighted by the pink ellipses, are 6.2, 8.1 and 9.9 meV for KNb_3Bi_5, $RbNb_3Bi_5$ and $CsNb_3Bi_5$, respectively. Given that the systems hold both inversion and time-reversal symmetries, as well as the continuous band gaps across the whole BZ, we can calculate the $\mathbb{Z}_2$ indices of each band around the Fermi level via analyzing the parity of the wave function at the eight TRIM points[23,28,39,45,46]. The calculated results are listed in Table 2. For KNb_3Bi_5 and $RbNb_3Bi_5$, the non-trivial topological invariant $\mathbb{Z}_2 = 1$ can be assigned to band-I. Differently, both the band-I and band-III of $CsNb_3Bi_5$ exhibit non-trivial topological index. For the traditional hexagonal materials, there are two unequal surfaces[28,45]. Due to the vdW interaction between adjacent layers, the easiest cleavage surface is (001) surface. We investigate the surface state on the (001) surface. The calculated surface states for KNb_3Bi_5 are plotted in Fig. 5a. One can see that the surface states exist both above and below the Fermi level, where the one above the Fermi level are rather complicated. When we enlarge the part above the Fermi level (the skyblue dash area in Fig. 5a), we can see that there are four surface states and the SS3 and SS4 states cross at 0.325 eV, as shown in Fig. 5b. The isoenergy contour (E = 0.325 eV) along the whole BZ and enlarged around M point are calculated and presented in Fig. 5c–d. Experimentally, the surface states below the Fermi level can be detected by traditional ARPES with a higher binding energy or removal of alkali metals, while the one above the Fermi level needs time-resolved ARPES. The cases of $RbNb_3Bi_5$ and $CsNb_3Bi_5$ are very similar to KNb_3Bi_5, as shown in Supplementary Figures 5 and 6. Considering the non-trivial topological index and the surface states in ANb_3Bi_5 (A = K, Rb, Cs), we can define this family materials as $\mathbb{Z}_2$ topological metals.

In summary, we have systematically investigated the coexistence of superconductivity and topological properties in the kagome metals of
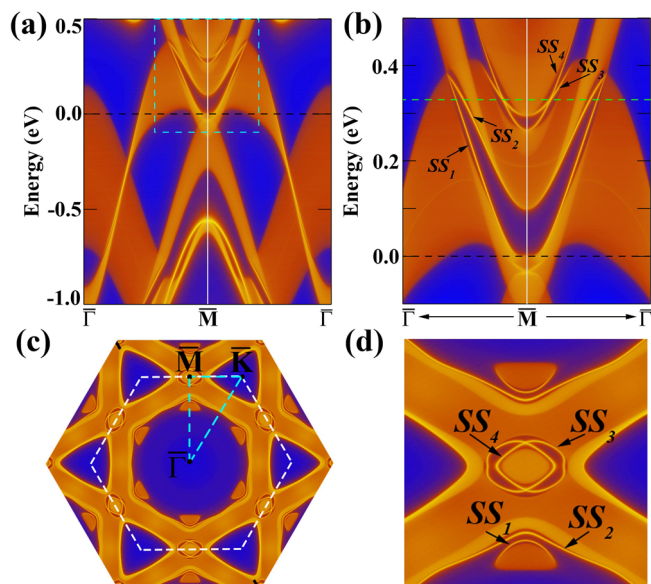
Fig. 5 | Surface states of KNb$_3$Bi$_5$. a Surface states of KNb$_3$Bi$_5$ along Γ-M-Γ direction. **b** Zoom-in surface states for the skyblue dash area in (**a**). Isoenergy contour ($E = 0.325$ eV) shows the green dash line in (**b**) along the whole BZ (**c**) and enlarged around M point (**d**).

ANb$_3$Bi$_5$ (A = K, Rb, Cs). The lattice stability is confirmed by the calculations of formation energy and phonon dispersion. Based on the Allen-Dynes modified McMillan formula, the superconducting critical temperature are predicted to be 2.11, 2.15 and 2.21 K for KNb$_3$Bi$_5$, RbNb$_3$Bi$_5$, and CsNb$_3$Bi$_5$, respectively. For ANb$_3$Bi$_5$ (A = K, Rb, Cs), the superconducting transition temperatures are rather similar, which can be attributed to the similar contributions of vibration modes to electron-phonon coupling and electronic orbital to the DOS at the Fermi level. Without SOC effect, the Dirac-like band crossing points, van Hove singularities and the flat band are observed. Similar to the AV$_3$Sb$_5$ family materials, the non-trivial electronic structures are confirmed via analyzing the parity of the wave function around the Fermi level at the TRIM points and the surface states in (001) plane, demonstrating that all three materials can be categorized as $\mathbb{Z}_2$ topological metals. The coexistence of superconductivity and nontrivial band structures in ANb$_3$Bi$_5$ (A = K, Rb, Cs) may offer more opportunities for the synthesis of kagome materials and the exploration of complex interactions between superconductivity and non-trivial topological states.

Methods

First-principles calculations settings

The crystal structural optimization and electronic structure calculation were preformed via the Quantum ESPRESSO package based on density functional theory (DFT)[47]. The interaction between the electrons and ionic cores were described by ultrasoft pseudopotentials[48], and the generalized gradient approximation (GGA) was used to treat the exchange-correlation interaction and parameterized by the Perdew-Burke-Ernzerhof functional[49]. Considering the quasi-two dimensional characteristic of crystal structures, the zero damping D3 van der Waals (vdW) correction was employed to describe the delicate vdW interaction between adjacent layers during crystal structural optimization[50], which is proved to be reasonable while describing the isostructural AV$_3$Sb$_5$ family materials[51,52]. The cutoff energy of wave functions and charge density were set as 80 Ry and 800 Ry, respectively. The Gaussian smearing method was used with a smearing parameter of $\sigma = 0.01$ Ry to evaluate the charge density. The Brillouin zone (BZ) was sampled with a $16 \times 16 \times 12$ k-points mesh for structural optimization, and all structures were fully relaxed until the force acting on each atom was $<10^{-5}$ Ry/Å and the convergence threshold on total energy was set to be 10^{-6} Ry.

Phonon-related calculations

Phonon dispersion curves were calculated based on density functional perturbation theory (DFPT)[53], where a denser $20 \times 20 \times 12$ k-point grid and a $5 \times 5 \times 3$ q-point grid were employed for the electron-phonon coupling calculations.

Surface states calculations

To investigate the projected surface states, we constructed a tight-binding model Hamiltonian by using maximally localized Wannier function (MLWF)[54,55], where the s orbitals of alkali metal A (A = K, Rb, Cs), d orbitals of the transition metal Nb atoms and the p orbitals of Bi atoms were used as the basis set. Then, we used the iterative Greens function as implemented in WannierTools package and the constructed Hamiltonian to calculate the surface states related properties[56,57].

Data availability

The authors declare that the data supporting the findings of this study are available within the paper and from the corresponding author upon reasonable request.

Code availability

The Quantum ESPRESSO package (v6.4.1) used to carry out the first-principles calculations is available under the GPLv2 license[47]. It can be downloaded from the following link: https://www.quantum-espresso.org/download-page. The WannierTools package used to calculate the surface states related properties is released under GPLv3[56,57], which can be downloaded from the following open source repository: https://github.com/quanshengwu/wannier_tools.

References

1. Balents, L. Spin liquids in frustrated magnets. *Nature* **464**, 199–208 (2010).
2. Yan, S. et al. Spin-liquid ground state of the S = 1/2 kagome heisenberg antiferromagnet. *Science* **332**, 1173–1176 (2011).
3. Han, T.-H. et al. Fractionalized excitations in the spin-liquid state of a kagome-lattice antiferromagnet. *Nature* **492**, 406–410 (2012).
4. Morali, N. et al. Fermi-arc diversity on surface terminations of the magnetic Weyl semimetal Co$_3$Sn$_2$S$_2$. *Science* **365**, 1286–1291 (2019).
5. Legendre, J. & Le Hur, K. Magnetic topological kagome systems. *Phys. Rev. Research* **2**, 022043 (2020).
6. Liu, D. F. et al. Magnetic Weyl semimetal phase in a kagom crystal. *Science* **365**, 1282–1285 (2019).
7. Wang, Q. et al. Large intrinsic anomalous Hall effect in half-metallic ferromagnet Co$_3$Sn$_2$S$_2$ with magnetic Weyl fermions. *Nat. Commun.* **9**, 3681 (2018).
8. Yu, S.-L. & Li, J.-X. Chiral superconducting phase and chiral spin-density-wave phase in a Hubbard model on the kagome lattice. *Phys. Rev. B* **85**, 144402 (2012).
9. Jiang, Y.-X. et al. Unconventional chiral charge order in kagome superconductor KV$_3$Sb$_5$. *Nat. Mater.* **20**, 1353–1357 (2021).
10. Ohgushi, K. et al. Spin anisotropy and quantum hall effect in the kagomé lattice: chiral spin state based on a ferromagnet. *Phys. Rev. B* **62**, R6065–R6068 (2000).
11. Li, H. et al. Electronic nematicity without charge density waves in titanium-based kagome metal. *Nat. Phys.* **19**, 1591–1598 (2023).
12. Nie, L. et al. Charge-density-wave-driven electronic nematicity in a kagome superconductor. *Nature* **604**, 59–64 (2022).
13. Liang, Z. et al. Three-dimensional charge density wave and surface-dependent vortex-core States in a Kagome superconductor CsV$_3$Sb$_5$. *Phys. Rev. X* **11**, 031026 (2021).

14. Ding, P. et al. Diagnosis of pairing symmetry by vortex and edge spectra in kagome superconductors. *Phys. Rev. B* **105**, 174518 (2022).

15. Ortiz, B. R. et al. New kagome prototype materials: discovery of KV_3Sb_5, RbV_3Sb_5, and CsV_3Sb_5. *Phys. Rev. Materials* **3**, 094407 (2019).

16. Fu, Y. et al. Quantum transport evidence of topological band structures of Kagome superconductor CsV_3Sb_5. *Phys. Rev. Lett.* **127**, 207002 (2021).

17. Ortiz, B. R. et al. Superconductivity in the $\mathbb{Z}_2$ kagome metal KV_3Sb_5. *Phys. Rev. Materials* **5**, 034801 (2021).

18. Yin, Q. et al. Superconductivity and normal-state properties of kagome metal RbV3Sb5 single crystals. *Chinese Phys. Lett.* **38**, 037403 (2021).

19. Yu, F. H. et al. Concurrence of anomalous hall effect and charge density wave in a superconducting topological kagome metal. *Phys. Rev. B* **104**, L041103 (2021).

20. Wang, Q. et al. Charge density wave orders and enhanced superconductivity under pressure in the Kagome metal CsV_3Sb_5. *Adv. Mater.* **33**, 2102813 (2021).

21. Yu, F. H. et al. Unusual competition of superconductivity and charge-density-wave state in a compressed topological kagome metal. *Nat. Commun.* **12**, 3645 (2021).

22. Chen, K. Y. et al. Double superconducting dome and triple enhancement of T_c in the Kagome superconductor CsV_3Sb_5 under high pressure. *Phys. Rev. Lett.* **126**, 247001 (2021).

23. Ortiz, B. R. et al. CsV_3Sb_5: A $\mathbb{Z}_2$ topological kagome metal with a superconducting ground state. *Phys. Rev. Lett.* **125**, 247002 (2020).

24. Kobayashi, S. & Sato, M. Topological superconductivity in dirac semimetals. *Phys. Rev. Lett.* **115**, 187001 (2015).

25. Qi, X.-L & Zhang, S.-C. Topological insulators and superconductors. *Rev. Mod. Phys.* **83**, 1057–1110 (2011).

26. Jiang, Y. et al. Screening promising CsV_3Sb_5-like kagome materials from systematic first-principles evaluation. *Chinese Phys. Lett.* **39**, 047402 (2022).

27. Yi, X.-W. et al. Large kagome family candidates with topological superconductivity and charge density waves. *Phys. Rev. B* **106**, L220505 (2022).

28. Si, J.-G. et al. Superconductivity and topological properties in the kagome metals CsM_3Te_5 (M = Ti, Zr, Hf): a first-principles investigation. *Phys. Rev. B* **106**, 214527 (2022).

29. Yi, X.-W. et al. Superconducting, topological, and transport properties of kagome metals $CsTi_3Bi_5$ and $RbTi_3Bi_5$. *Research* **6**, 0238 (2023).

30. Yang, H. et al. Titanium-based kagome superconductor $CsTi_3Bi_5$ and topological states. *arXiv* https://arxiv.org/abs/2209.03840.

31. Yang, J. et al. Observation of flat band, dirac nodal lines and topological surface states in kagome superconductor $CsTi_3Bi_5$. *Nat. Commun.* **14**, 4089 (2023).

32. Liu, B. et al. Tunable van hove singularity without structural instability in kagome metal $CsTi_3Bi_5$. *Phys. Rev. Lett.* **131**, 026701 (2023).

33. Nie, J.Y. et al. Pressure-induced double-dome superconductivity in kagome metal $CsTi_3Bi_5$. *arXiv* https://arxiv.org/abs/2308.10129.

34. McMillan, W. L. Transition temperature of strong-coupled superconductors. *Phys. Rev.* **167**, 331–344 (1968).

35. Allen, P. B. & Dynes, R. C. Transition temperature of strong-coupled superconductors reanalyzed. *Phys. Rev. B* **12**, 905–922 (1975).

36. Böhm, B. & Klemm, W. Zur kenntnis des verhaltens der alkalimetalle zueinander. *Z. Anorg. Allg. Chem.* **243**, 69–85 (1939).

37. Goldschmidt, H. J. & Brand, J. A. The constitution of the chromium-niobium-molybdenum system. *J. Less Common Met.* **3**, 44–61 (1961).

38. Giessen, B. C. et al. Metastable indium-bismuth phases produced by rapid quenching. *Aime. Met. Soc. Trans.* **239**, 883–889 (1967).

39. Si, J.-G. et al. Charge density wave and pressure-dependent superconductivity in the kagome metal CsV_3Sb_5: a first-principles study. *Phys. Rev. B* **105**, 024517 (2022).

40. Duong, D. L. et al. Ab initio computation of the transition temperature of the charge density wave transition in $TiSe_2$. *Phys. Rev. B* **92**, 245131 (2015).

41. Ku, R. et al. Ab initio investigation of charge density wave and superconductivity in two-dimensional Janus $2H/1T$-MoSH monolayers. *Phys. Rev. B* **107**, 064508 (2023).

42. Wei, M. J. et al. Manipulating charge density wave order in monolayer $1T - TiSe_2$ by strain and charge doping: a first-principles investigation. *Phys. Rev. B* **96**, 165404 (2017).

43. Kang, M. et al. Twofold van Hove singularity and origin of charge order in topological kagome superconductor CsV3Sb5. *Nat. Phys.* **18**, 301–308 (2022).

44. Fu, L. et al. Topological insulators in three dimensions. *Phys. Rev. Lett.* **98**, 106803 (2007).

45. Shi, L.-T. et al. Topological and superconducting properties in bilayer kagome metals YT_6Sn_6 (T = V, Nb, Ta). *Phys. Rev. B* **107**, 184503 (2023).

46. Ahsan, T. et al. Prediction of strong topological insulator phase in kagome metal RV_6Ge_6. *Phys. Rev. Materials* **7**, 104204 (2023).

47. Giannozzi, P. et al. QUANTUM ESPRESSO: a modular and open-source software project for quantum simulations of materials. *J. Phys. Condens. Matter* **21**, 395502 (2009).

48. Vanderbilt, D. Soft self-consistent pseudopotentials in a generalized eigenvalue formalism. *Phys. Rev. B* **41**, 7892–7895 (1990).

49. Perdew, J. P. et al. Generalized gradient approximation made simple. *Phys. Rev. Lett.* **77**, 3865–3868 (1996).

50. Grimme, S. et al. A consistent and accurate ab initio parametrization of density functional dispersion correction (DFT-D) for the 94 elements H-Pu. *J. Chem. Phys.* **132**, 154104 (2010).

51. Tan, H. et al. Charge density waves and electronic properties of superconducting Kagome metals. *Phys. Rev. Lett.* **127**, 046401 (2021).

52. Liu, Z. et al. Charge-density-wave-induced bands renormalization and energy gaps in a kagome superconductor RbV_3Sb_5. *Phys. Rev. X* **11**, 041010 (2021).

53. Baroni, S. et al. Phonons and related crystal properties from density-functional perturbation theory. *Rev. Mod. Phys.* **73**, 515–562 (2001).

54. Souza, I. et al. Maximally localized wannier functions for entangled energy bands. *Phys. Rev. B* **65**, 035109 (2001).

55. Marzari, N. et al. Maximally localized wannier functions: theory and applications. *Rev. Mod. Phys.* **84**, 1419–1475 (2012).

56. Sancho, M. P. L. et al. Highly convergent schemes for the calculation of bulk and surface green functions. *J. Phy. F Met. Phy.* **15**, 851 (1985).

57. Wu, Q. et al. WannierTools: an open-source software package for novel topological materials. *Comput. Phys. Commun.* **224**, 405–416 (2018).

Acknowledgements

Author contributions

J.S. and S.M. initiated the idea of this project. J.S. performed the simulations, data analysis and writing-original draft. L.S. performed the data curation, check and revision. B.C. and H.Y. performed the formal analysis. J.X., M.L. and S.M. supervised and revised this project. All authors discussed and analyzed the results of the paper. J.S. and L.S. contributed equally to this work.

Competing interests

The authors declare no competing interests.

Additional information

Supplementary information The online version contains supplementary material available at https://doi.org/10.1038/s41524-024-01291-w.

Correspondence and requests for materials should be addressed to Jiyu Xu, Miao Liu or Sheng Meng.

Reprints and permissions information is available at http://www.nature.com/reprints

Publisher's note Springer Nature remains neutral with regard to jurisdictional claims in published maps and institutional affiliations.